Capturing nonlinear time-dependent aircraft dynamics using a wind tunnel manoeuvre rig

Abstract

This paper considers a novel multi-degree-of-freedom dynamic manoeuvre rig, with the aim of assessing its potential for capturing aircraft model nonlinear time dependent dynamics in the wind tunnel. The dynamic manoeuvre rig capabilities are demonstrated via a series of experiments involving a model aircraft in a closed section low-speed wind tunnel. A series of open loop experiments show that the aircraft model exhibits nonlinear time dependent dynamics. This nonlinear behaviour manifests itself as limit cycle oscillations that increase in complexity with the number of degrees-of-freedom in which the aircraft is allowed to move. Two real-time closed loop control experiments further illustrate the manoeuvre rig potential: first, using a pitch motion configuration, an experiment is conducted to investigate the limit cycle behaviour in more detail, allowing the stability properties of the pitch oscillations to be assessed; secondly, using a 5-DOF motion configuration, the test motion envelope is extended by using a compensating feedback control law to track the aircraft's roll motion. Together, these experiments demonstrate the manoeuvre rig potential to reveal aircraft nonlinear and unsteady phenomena.

Keywords: wind tunnel, dynamic testing, limit cycle oscillations, bifurcations, nonlinear dynamics, aerodynamic hysteresis

1. Introduction

Since the 1920's, wind tunnel dynamic testing has been recognised as an essential tool for flight dynamics. Ever since, the challenge has been to capture the behaviour of a model of the aircraft while mounted in the tunnel. As an early example, in 1922, a continuous rotation balance was developed by Relf and Lanvender at the Royal Aircraft Establishment in the UK, first for measuring rolling moment [1] and then both the pitching and yawing moments due to angular velocity of roll [2]. Another example is the work by Nicolaides and Eikenberry who measured the static and dynamic aerodynamic characteristics of statically stable and unstable missiles using two free oscillating rigs, a 1-Degree-of-Freedom (DOF) pitch motion rig and a 3-DOF roll, pitch and yaw motion rig [3]. In 1981, Orlik-Ruckemann presented a review of the existing wind tunnel techniques for determining dynamic stability parameters [4], including both unconstrained models capable of providing thrust in free-flight and, more commonly, models that have no thrust capability and hence require constraints. More recently, Huang and Wang presented a summary of the historic development of dynamic testing techniques and reported the state of the art capabilities of dynamic wind tunnel rigs [5], concluding that novel constraining mechanisms that allow the model to have multi-DOF motions have the potential to significantly enhance capabilities for dynamic testing.

Concentrating on captive models, a forced oscillation rig has been used at the $14' \times 22'$ subsonic wind tunnel at NASA Langley Research Center to study how unsteady aerodynamics affect aircraft flight dynamics [6] and then to estimate the unsteady aerodynamic parameters [7] of a 10% scale F-16XL model. Using the techniques developed for fighter aircraft, research has been carried out to characterise the non-linear and unsteady aerodynamic effects of large transport aircraft in conditions beyond the normal operating envelope [8–16]. Modelling of post-stall flight dynamics and spin dynamics of large transport aeroplanes using data obtained from static, forced oscillation and rotary balance wind tunnel experiments has been performed by NASA [14]. Moreover, using static and forced oscillation wind tunnel experiments, a mathematical model which describes the longitudinal dynamics [15] and the lateral-directional dynamics [16] was produced. Owens *et al.* provided an overview of the dynamic testing facilities available at NASA Langley Research Centre [17].

More recently, the lift and drag forces of a generic unmanned combat air vehicle were characterised using static and forced oscillation testing and then compared to CFD results by Cummings *et al.* working at the Department of Aeronautics at the USAF [18]. In the Central Aerohydrodynamic Institute (TsAGI) in Russia, wind tunnel experiments were carried out to investigate the effect of icing on the longitudinal steady and unsteady aerodynamic characteristics of an aircraft model [19]. In the Lu Shijia Laboratory at the Beihang University in China, the aerodynamic characteristics of a delta wing at high angles of attack were studied through pitching oscillation experiments in a water channel [20]. In the German-Dutch Wind Tunnels, a novel dynamic testing rig known as the Model Positioning Mechanism (MPM) was developed for standard static testing, ground effect simulation, manoeuvre simulation and forced oscillation testing. The MPM allows for 6-DOF motions of model aircraft rigidly mounted to a sting and has been used to identify dynamic derivatives [21] and to simulate complex manoeuvres of a X-31 model [22]. It has also allowed the deployment trajectories of rigid bodies launched from a generic military transport aircraft model to be identified [23] and for static and forced oscillation testing of a generic swept wing unmanned combat air vehicle [24–29]. A rig developed at Cranfield University allows for dynamic testing of aircraft models in roll, pitch, yaw and vertical translation and has been used to study the stability and control characteristics of a 1/12 scale BAe Hawk model for small amplitude motions [30, 31]. Most of these techniques are used for aerodynamic characterisation utilising a relatively low number of DOF. However, modelling the dynamics of an aircraft is complicated by factors such as unsteady (time-dependent) effects, aircraft configuration dependence (particularly important in the nonlinear regime, such as at high angle of attack) and the difficulty in accommodating coupled (multi-DOF) motions. This results in a need for complementary wind tunnel techniques for multi-DOF aerodynamic characterisation and flight control law development and evaluation.

The purpose of this type of enhanced dynamic testing is to ensure that the complex behaviour of the aircraft wind tunnel model can be observed across a range of conditions. The experiments would not only generate data that can be used to fit a mathematical model but, importantly, they would provide a means of developing a sound understanding of the aerodynamic flow phenomena underlying the behaviour and to explore their dependencies/sensitivities to operating conditions. This is a highly beneficial precursor to fitting a mathematical model to the measured responses and to subsequently designing control laws to modify the aircraft model response to inputs. It is this exploration of the behaviour of the aircraft model in the presence of nonlinear/unsteady aerodynamic reactions that is the topic of this paper.

At the University of Bristol (UoB), the ‘manoeuvre rig’ has been developed specifically to extend ground testing capabilities for effective flight characteristics observation and prediction, control law design and evaluation and increased wind-tunnel testing productivity. Using the rig, the model is attached via a gimbal to an arm which itself is attached to ground via a second gimbal. It allows the aircraft model to be tested in up to five degrees of freedom with motions imparted via its own control surfaces, and with an aerodynamically-driven compensation unit attached to the rig arm. This unit allows forced oscillation tests and the potential for dynamic compensation of the rig motions so that the model can behave, in principle, as if it were in free motion under those DOFs. The resulting 'physical simulation' allows for the observation of aircraft behaviour, including the influence of nonlinear and/or time-dependent aerodynamics such as that responsible for the onset of upset/departure; and the motion data from such tests – or from forced motions driven by the rig compensator system – can then be used to carry out parameter estimation for mathematical model development. A similar 5-DOF rig has been developed at IIT Kanpur to simulate free flight manoeuvres of a delta-winged aircraft model in a wind tunnel and to estimate simulation model parameters [32].

In this paper, we demonstrate the potential of the manoeuvre rig to observe nonlinear time dependent flight dynamics and how, by systematically realising different DOFs, this behaviour can be measured and studied. It is anticipated that the data the novel rig can capture will enable researchers to better understand the nonlinear aerodynamics and flight behaviour of an aircraft, something that is discussed here for a series of example tests, and allow limitations in any numerical model of the aircraft to be identified. It could also be used to enhance or fit a numerical model using parameter estimation, or to determine suitable feedback control approaches to improve the nonlinear behaviours observed but this is beyond the scope of the paper. Through a series of open-loop and closed-loop experiments, we illustrate how it becomes possible to observe this nonlinear behaviour and to assess the dynamical structure of said aircraft in highly complex motion configurations. After presenting the rig and broadly discussing its capabilities in Section 2, we build on previous work obtaining aerodynamic data [33] and characterising the oscillatory longitudinal pitch and heave motions of an aircraft model [34] by demonstrating how equilibria and limit-cycle oscillations (LCO) in heave and pitch can be identified along with the separatrix between solution types (Section 3). We demonstrate that the robustness of such oscillations as further DOFs are added can be investigated and reveal that for the aircraft model investigated there is a strong pitch-roll coupling (Section 4). Section 5 discusses the potential insights than can be gained when 5 DOF are unlocked and looks at the use of compensating feedback control laws for tracking roll motion. This discussion is then extended to consider the potential for using force measurements to further enhance its control. Finally, Section 6 provides concluding remarks.

2. Experimental Platform

In discussing the potential of dynamic testing of captive models in the wind tunnel, we select the UoB manoeuvre rig as a case-study test facility and consider the types of testing that can be conducted, giving some example results. In this section we introduce the manoeuvre rig and then overview the types of testing it, and similar rigs, can be used for and the insights these can provide.

Using the manoeuvre rig the aircraft model is supported on a 3-DOF gimbal, the model gimbal, which can allow roll, pitch and yaw motions relative to the gimbal mount. This gimbal is attached to an arm which itself is mounted – via another 3-DOF gimbal, the arm gimbal – on a fixed vertical strut bolted to a rigid structure below the tunnel working section floor. This arm gimbal provides arm roll, arm pitch and arm yaw (see Figure 1a). The arm pitch and arm yaw provide approximate aircraft heave and aircraft sway motions as shown in Figures 2d to 2f. Note that due to the finite arm length, the model gimbal moves in an arc; this contributes kinematic coupling between the rig motions and those of the aircraft model. The 3-DOF model gimbal sits at the upstream end of the arm (see Figure 1a), with the rig compensator located at the downstream end. This gimbal connects the arm to the aircraft and allows for aircraft roll, aircraft pitch and aircraft yaw, as shown in Figures 2a to 2c. Whilst both gimbals incorporate roll degrees of freedom, they rotate about different axes: the model body axis for the arm gimbal and arm longitudinal axis for the arm gimbal; the latter will make additional contributions to the roll and yaw components of rotation in model body axes. Despite the availability of six rig DOFs, these are considered to imbue the model itself with a maximum of 5 DOFs: there is no unconstrained fore-aft model degree of freedom (its translations in this sense are components of motion along the spherical surface prescribed by arm rotations in yaw and pitch). Note that the gimbals allow for motions about individual axes to be locked so that the rig can be configured with DOFs ranging from zero (static) to five.

An approximate BAe Hawk aircraft model was used to carry out the experiments presented in this paper. A representation of the Hawk model mounted on the manoeuvre rig can be seen in Figure 1a. Figure 1b shows the rig when installed in the $7' \times 5'$ closed section wind tunnel. A safety cable system can be observed in the background: this is used to restrict the rig's sway and heave motions.

The 3-DOF arm gimbal angular displacements are measured using poten-

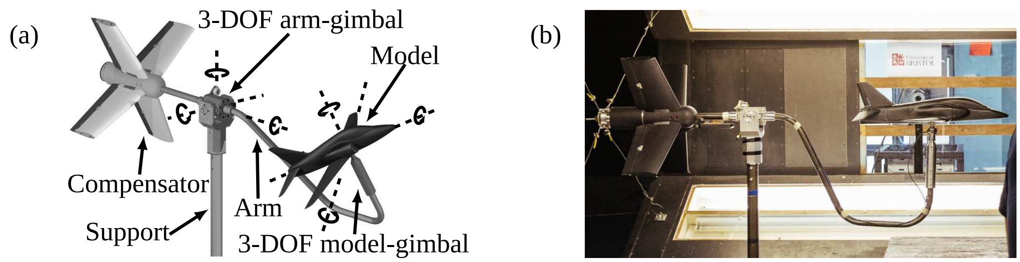

Figure 1: The University of Bristol's manoeuvre rig: (a) 6-DOF manoeuvre rig schematic and (b) rig mounted in the $7' \times 5'$ closed section wind tunnel.

tiometers, while those of the 3-DOF model gimbal and the control surfaces from the compensator are measured using absolute digital encoders. The compensator can be used to produce additional loads which can be tailored to carry out forced rotation/oscillation tests, to reduce inertial, aerodynamic or kinematic coupling between the aircraft and the arm (physical simulation) and to extend the rig's motion envelope for control law evaluation. The aircraft orientation relative to tunnel (Earth) axes can also be obtained from an inertial measurement unit (IMU) mounted in the aircraft model. The angular displacements of the aircraft model control surfaces are measured using the potentiometers embedded in the servo motors. The characteristics of the rig and aircraft, kinematic equations and dynamic model have been reported previously [33, 35–38].

The rig can be used for various types of testing, which are classified for convenience as follows.

Rotational DOFs only; model gimbal free with arm gimbal locked:

- This can range from 1-DOF to 3-DOF, depending which model gimbal axes are locked and which are free. Motions are driven by aircraft model control surfaces or potentially by an external disturbance such as a gust generator. Note that forced-oscillation experiments can be conducted using the model

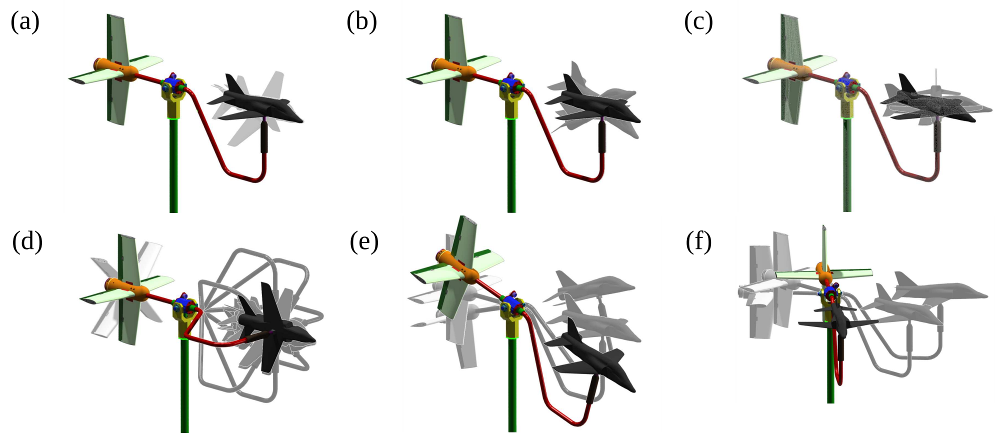

Figure 2: Manoeuvre rig 6-DOF motions: (a) aircraft roll, (b) aircraft pitch, (c) aircraft yaw, (d) aircraft extended roll, (e) aircraft heave and (f) aircraft sway.

control surfaces to acquire dynamic stability derivatives [39, 40], as well as unsteady aerodynamic characteristics [19].

- A single-DOF pitch-only test is often a useful starting point for dynamic testing: motions reflect the approximate short period mode for a conventional aircraft model configuration. Using all 3 DOFs reveals behaviour indicative of the 'fast' modes (short period, Dutch roll, roll subsidence).

- Tests can examine stability of the modes and, where roll and/or yaw are free along with pitch, indicate asymmetry and coupling of longitudinal with lateral-directional dynamics. This can be done by 'flying' the model with random or specified control surface inputs and recording the responses – so-called 'physical simulation'.

- Aerodynamic models providing dependence of loads on α, β and rotation rates can be derived using parameter estimation.

- Angular rate and stability augmentation controllers can be implemented, evaluated and tuned.

- If a load cell is incorporated into the rig, between the end of the arm and the aircraft gimbal mount, then static and dynamic lift coefficients can be measured about different equilibrium (trim) points.

Rotational DOFs only; model gimbal rotational DoFs free with arm gimbal unlocked in roll:

- The arm and gimbals are designed so that the axis of arm rotation in roll passes through the model gimbal centre; therefore, freeing this degree of freedom, in addition to any of the model-gimbal DOFs, provides an additional rotation – about the arm axis – and no associated translation of the model. This does not add any further DOFs over and above those of the model gimbal but, importantly, the arm can rotate continuously whereas the model-gimbal rotation in roll is constrained by hard limits ($\pm 42^\circ$ at zero pitch angle). Video 01 (see supplementary material) shows a 3-DOF example experiment in which the aircraft is free to move in roll, pitch, and yaw, with the motion driven by its control surfaces. The manoeuvre rig tracks the roll motion using feedback control to extend the aircraft's roll motion envelope [36].

- In this configuration, the rig compensator control surfaces can be used to drive the arm roll (forced rotation/oscillation); alternatively, where model control surfaces are used to drive model motions, the compensator must be used to provide for roll responses larger than the model gimbal limits. This is explored in Section 5.

- Physical simulation, aerodynamic model parameter estimation and control law evaluation can all be conducted as in the rotation-only tests (with the additional option of forced motion in roll via the compensator). Similarly, if a load cell is fitted between the arm and model gimbal then force and moment measurements can be made.

Rotational and translational DOFs, model and arm gimbals unlocked in at least one DOF:

The same types of testing as above can be conducted, with one or both 'translational' DOFs free, namely model heave through arm pitch and model sway through arm yaw. The latter introduce further options for compensator-forced model motions or rig compensation. Application of rig compensation requires measurement of the reaction force between the aircraft model and the rig arm (via a load cell); the effect of rig geometric constraints, kinematics and inertial effects (and in principle also aerodynamic and structural dynamics) on the rig-aircraft dynamics are then miminised by feeding back the reaction force to the aerodynamic compensator [38].

- A 2-DOF test with model-gimbal pitch and arm pitch allows a closer approximation to the short period dynamics of a free aircraft model than rotation only. It also allows for separate estimation of $\dot{\alpha}$ and q stability derivatives. Furthermore, even without a load cell, static lift loads can be estimated through the compensator model when the latter is used to balance the system [41]. When the model is driven by its onboard control surfaces or excited by an external device such as a gust generator, the compensator can be used to apply compensation for the influence of the rig on model behaviour or alternatively to force model motions (e.g. for parameter estimation).

- A 2-DOF test with model-gimbal yaw and arm sway mirrors the above in the lateral-directional sense.

- All the aforementioned configurations can be combined to form various 2-, 3-, 4- and 5-DOF test condition. The more degrees of freedom given to the system, the more representative the coupling between longitudinal and lateral-directional motions and the closer the responses to that of a free-flying model – including the onset of phenomena such as stall asymmetry and upset. As before, the behaviour of the aircraft model can be explored by physical simulation and parameter estimation, control law design, etc. carried out. An example of this is shown in Video 02 (see supplementary material), where the rig is set up in a 5-DOF configuration, i.e. aircraft roll, pitch, yaw and approximate heave and sway motions, with extended rig-roll motion. In this case the aircraft control surfaces drive the motion, while the aerodynamic compensator is used to compensate the rig roll dynamics via feedback control. Note that as part of the aircraft's controller roll rate feedback is used (measured using the IMU mounted in the aircraft model), and any high-frequency motion is likely to be in response to process (turbulence) and/or measurement noise.

Recent applications of the rig have been aimed at assessing the level of interaction between the different DOF as nonlinear phenomena appear, exploring the compensation of roll motion using the aerodynamic compensator (Figure 1a) [36], investigating aerodynamic hysteresis utilising a feedback control law to track the aircraft's equilibria [41] and studying the effects of geometric constraints on the coupled rig/aircraft dynamics by feedback of load cell reaction force measurements to the compensator control surfaces [38].

Next, Sections 3 and 4 present experimental results exploring nonlinear time dependent flight dynamics and how these dynamics differ as different DOF configurations are used.

3. Aircraft Pitch Equilibria and Limit Cycle Oscillations

This section presents results from experiments carried out to explore the LCO behaviour in a 1-DOF aircraft pitch configuration. Such tests can reveal the influence of complex flow phenomena on longitudinal behaviour, including changes in stability, associated bifurcation phenomena leading to LCO and resulting hysteresis effects. Similar 1-DOF tests have been carried out before (e.g. [34]) but this was prior to the rig refinements which provide more accurate measurements of control surface angles and model rotation rates, hence allowing a more thorough study. Then, building on these results, the investigation is extended with a series of tests where a feedback control law is used to study the stability characteristics of the equilibria and LCO.

Pitch LCO for this aircraft model were first reported by Kyle [42], where a pendulum rig in a 1-DOF pitch motion configuration was used to study the dynamics of the aircraft model. The LCO behaviour was modelled by Davison [43] using hyperbolic tangent growth/decay functions to transition from/to equilibria and sinusoidal functions to model the shape of the LCO. Subsequently, using the earlier manoeuvre rig configuration[1] in 1-DOF and 2-DOF configurations, analysis and modelling of the LCO behaviour was carried out by Pattinson using continuation and bifurcation tools [34]. This involved the identification of parameters

[1]This configuration did not provide direct measurements of the model control surfaces and rotational rates (and the aircraft gimbal was 2-DOF rather then 3-DOF).

in an unsteady aerodynamic model, along with a friction model, incorporated in the equations of motion so as to provide as close a match as possible to the limit cycle characteristics and bifurcationary structure observed in the experiments.

More recently, experimental exploration of the LCO behaviour using an updated version of the manoeuvre rig was carried out [37]. These experiments were conducted to further explore the lateral-directional interaction between the different degrees of freedom as nonlinear phenomena appear (first observed by Pattinson *et al* [33], despite the absence of direct measurements of the model aileron δ^m_{ail}, elevator δ^m_{ele} and rudder δ^m_{rdd} or rotation rates p_m, q_m, r_m) and to explore roll motion compensation using the aerodynamic compensator control surfaces.

All the results presented throughout this paper are from experiments carried out in the $7' \times 5'$ closed circuit wind tunnel at the University of Bristol at a wind speed of $30\,\mathrm{m/s}$. Note that the manoeuvre rig can be installed and operated in either the $7' \times 5'$ closed-section tunnel or an open-jet, both available at the University's wind tunnel facility. The former was chosen because this particular tunnel has better flow quality than the open-jet one. It will be shown that the rig refinements and incorporation of feedback control methods provide improved results than in previous studies: in particular, the effects of unsteady flow phenomena are able to be observed in more detail, including separatrices between stable solutions and a more complex LCO structure.

3.1. 1-DOF Aircraft Pitch LCO

First consider the configuration in which the aircraft is free to move in pitch and the arm is locked in its horizontal position, i.e. the 1-DOF aircraft pitch configuration (Figure 2b). Figure 3a shows the response of the Hawk model in the time domain when the elevator angle demand is ramped slowly from zero to $-28°$

and then back to zero. This is a logical first step in this type of testing, where a control surface is used to provide inputs to model motion: the response to a sufficiently slow ramp-type input can be regarded as quasi-steady and the measured results are therefore able to be presented both as time histories and in a less usual format – an experimental bifurcation diagram.

The elevator response δ^m_{ele} is shown in Figure 3a(i), with the aircraft pitch angle θ_m and the pitch rate q_m shown in Figures 3a(ii) and 3a(iii), respectively. Note that in this 1-DOF configuration, θ_m is the model angle of attack. Five regions where pitch LCO occur can be identified by studying the θ_m and q_m plots, namely in the periods $t \approx 50$ s, $t \approx 100$ s, $120\,\text{s} \leq t \leq 180$ s, $300\,\text{s} \leq t \leq 350$ s and $t \approx 400$ s. In the following discussion the first and fifth of these regions will be referred to as low α LCO, and the second, third and fourth regions as high α LCO. The aircraft high α LCO response while in this configuration is presented in the supplementary video file Video 03.

An alternative way of studying the LCO behaviour is by presenting the system steady state dynamics in the form a bifurcation diagram. Note that equilibrium (fixed-point) solutions shown in bifurcation diagrams may be regarded as trimming points [19]. For an overview on bifurcation theory and its application to aircraft dynamics analysis the reader is referred to Goman *et al* [44], Thompson and Macmillen (eds.) [45] and Sharma *et al* [46]. Using the data shown in Figure 3a, the aircraft elevator is taken as the bifurcation parameter. Taking only the points where $|q_m| \leq 5\,°/\text{s}$, i.e. where the rate can be thought of as approximately the zero-rate points, an experimental bifurcation diagram is obtained as shown in Figure 3b. Here, the data points represent stable equilibria or limit cycle minimum and maximum amplitudes. By applying a smoothing post-processing lag-free fil-

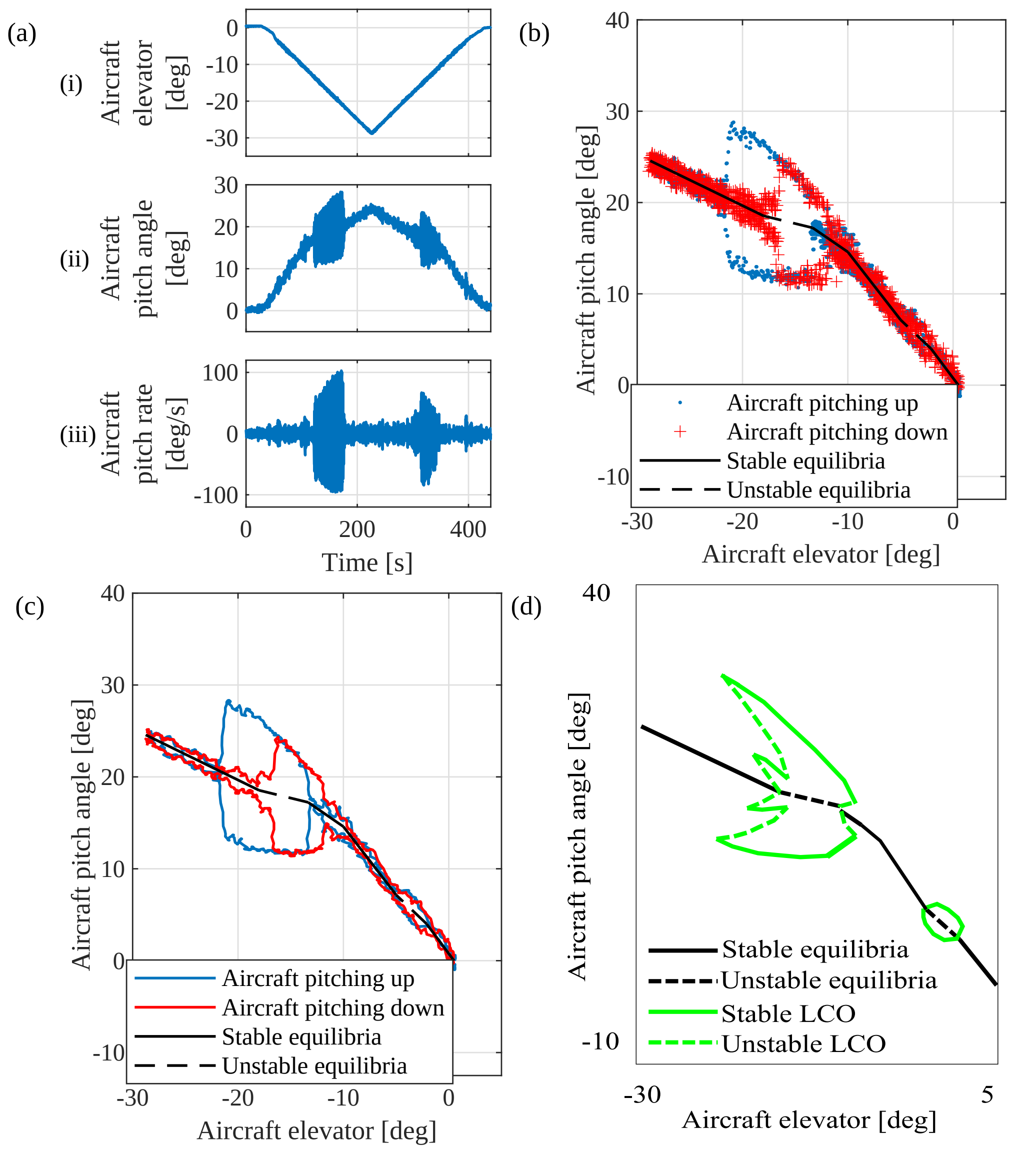

Figure 3: 1-DOF aircraft model pitch experimental data: (a) time histories, (b) point cloud bifurcation diagram, (c) smoothed bifurcation diagram and (d) likely structure of bifurcation diagram.

ter to this data, some of the features of the LCO are easier to observe. This is shown in Figure 3c. The filter used here was formulated by Jategaonkar and it is based on a 15-point symmetric low-pass digital filter developed by Spencer [47]. In Figures 3b and 3c data in blue represent values corresponding to a decreasing aircraft elevator δ^m_{ele} sweep, while data in red represents values corresponding to an increasing one. The black solid line represents stable equilibria while the black dashed line represents unstable equilibria; these illustrative lines were superimposed onto the experimental data to aid its interpretation (no attempt was made in this work to determine the unstable solutions experimentally).

The first of these features is a small LCO at low α over the region $-5° \leq \delta^m_{ele} \leq -2°$ and $3° \leq \theta_{ele} \leq 7°$, corresponding to those observed around $t \approx 50$ s and $t \approx 400$ s in Figure 3a. The second LCO, the high α LCO, can be observed over the region $-22° \leq \delta^m_{ele} \leq -10°$. Aerodynamic hysteretic behaviour exhibited by the aircraft model used for this test can be observed over the region $-22° \leq \delta^m_{ele} \leq -16°$ and $-13° \leq \delta^m_{ele} \leq -11.5°$. In this region the large amplitude LCO is only observed during the decreasing elevator deflection part of the test. When studying in greater detail the plot corresponding to the aircraft elevator increasing deflection in the region $-18° \leq \delta^m_{ele} \leq -16°$, evidence of an 'inner' LCO can be observed. The characteristics of this LCO are discussed in Section 3.2. Note that the inner limit cycle might extend further in the pitching up direction due to hysteresis. It would be possible to investigate this by switching the experiment to a pitch up ramp at the point where this solution is reached and then following it, but this was not part of the testing schedule for this study.

Based on the features described before, the likely structure of the bifurcation diagram is sketched in Figure 3d. The sketch shows five features: stable equilibria in solid black line, unstable equilibria in dashed black line, stable LCO branches in solid green line (at low and high α), high α unstable LCO branches in dashed green line and a stable inner branch also in solid green line.

The two LCO regions — one around $\theta = 5°$ (low α) and the other starting at $\theta = 15°$ (high α) — have been reported before [34, 42, 43]. However, a new feature has been identified here: the results suggest the existence of an inner LCO within the hysteretic region of the high α LCO. The hysteresis phenomena in this region were studied in [41] and found to be associated with an asymmetric separated flow structure on the wings. It was shown in [35], by testing at non-zero model yaw angles, that this hysteretic behaviour is sustained over a range of sideslip angles (although their extent does vary noticeably); this suggests that the existence of these structures is robust to the flow conditions but their characteritics are dependent on them. The low α LCO, on the other hand, disappears for larger sideslip conditions, indicating that it may be linked to loss of longitudinal stability due to shadowing of the tailplane. Results from a similar test but with non-zero *rig* yaw angles will be shown in Section 4.1.

3.2. 1-DOF Aircraft Pitch: Equilibria & LCO Stability

To investigate the characteristics of the LCO in more detail and to demonstrate the manoeuvre rig's capabilities for aircraft control law design and aerodynamic modelling, a series of closed loop tests using the Hawk model installed on the manoeuvre rig in a 1-DOF model pitch configuration were performed. In these tests, the Hawk model elevator was used as the control variable. A feedback control law implemented in Simulink® was used to both set the nominal pitch angle and then stabilise the aircraft pitch motion. A similar method to the one presented here was used by Gong *et al* [41] to track the equilibria of pitch-only dynamics. In this work, the test is used to reveal the more complex LCO structures and the stability characteristics of both the equilibria and LCO. The design of this feedback control law is summarised as follows.

In a 1-DOF pitch configuration, the aircraft angle of attack α_m is equal to the aircraft pitch angle θ_m and the aircraft pitch dynamics can be described by

$$\begin{aligned}\left(m_m \ell_{z_m}^2 + I_{yy}\right)\dot{q}_m &= -f\left(q_m\right) - m_m g \ell_{z_m}\sin(\theta_m) + \\ &\quad \frac{1}{2}\rho V^2 S_m \bar{c}_m C_M\left(\theta_m,\, q_m,\, \delta_{ele}^m\right) + w\left(t\right)\end{aligned} \tag{1}$$

where m_m is the aircraft model mass, ℓ_{z_m} is the (small) vertical offset of the model centre of gravity (CG) from the gimbal centre of rotation, I_{yy} is the pitch moment of inertia of the model about its CG, $\dot{q}_m$ the pitch acceleration, $f\left(q_m\right)$ the model gimbal pitch friction, g the acceleration due to gravity, ρ the air density, V the wind speed, S_m and $\bar{c}_m$ the aircraft model wing reference area and mean aerodynamic chord respectively, C_M the aerodynamic pitching moment coefficient and $w\left(t\right)$ the moment contribution due to wind tunnel turbulence, with both q_m and δ_{ele}^m previously defined in Section 3. Note that $w\left(t\right)$ represents stochastic process noise. To account for the uncertainty on this parameter and to evaluate both the robustness and repeatability of the results presented in this section, perturbations were added by means of switching on/off the controller and via elevator step inputs with different magnitudes.

Additionally, considering the aerodynamic pitching moment coefficient as a combination of linearly independent functions, gives

$$C_M\left(\theta_m,\, q_m,\, \delta_{ele}^m\right) = C_{M_0}\left(\theta_m\right) + C_{M_{q_m}}\left(\theta_m,\, q_m\right) + C_{M_{\delta_{ele}^m}}\left(\theta_m,\, \delta_{ele}^m\right) \tag{2}$$

Here, $C_{M_{q_m}}$ and $C_{M_{\delta_{ele}^m}}$ represent the dependence of C_M on q_m and δ_{ele}^m respectively.

Then, by collecting terms, equation (1) can be reformulated as

$$\left(m_m \ell_{z_m}^2 + I_{yy}\right) \dot{q}_m = g\left(\theta_m\right) + h\left(\theta_m,\ q_m\right) + u\left(\theta_m,\ \delta_{ele}^m\right) + w\left(t\right) \tag{3}$$

where

$$\begin{aligned}
\text{Stiffness}\left\{\quad g\left(\theta_m\right)\right. &= \frac{1}{2}\rho V^2 S_m \bar{c}_m C_{M_0}\left(\theta_m\right) - m_m g \ell_{z_m} \sin(\theta_m) \\
\text{Damping}\left\{\quad h\left(\theta_m,\ q_m\right)\right. &= \frac{1}{2}\rho V^2 S_m \bar{c}_m C_{M_{q_m}}\left(\theta_m,\ q_m\right) - f\left(q_m\right) \\
\text{Control input}\left\{\quad u\left(\theta_m,\ \delta_{ele}^m\right)\right. &= \frac{1}{2}\rho V^2 S_m \bar{c}_m C_{M_{\delta_{ele}^m}}\left(\theta_m,\ \delta_{ele}^m\right) \quad .
\end{aligned}$$

By substituting $q_m = 0$ and $\dot{q}_m = 0$ into equation (3) and neglecting any wind tunnel turbulence, the equilibria of the system can be expressed as

$$u\left(\bar{\theta}_m,\ \bar{\delta}_{ele}^m\right) = -g\left(\bar{\theta}_m\right) \tag{4}$$

where the over bar indicates equilibrium values. From (4) it can be deduced that, in the absence of external perturbations, any given aircraft model elevator deflection results in an equilibrium aircraft pitch angle.

Hence, tracking of the equilibria is achieved by defining the control law

$$u\left(\theta_m,\ \delta_{ele}^m\right) = u\left(\hat{\delta}_{ele}^m\right) + k_{q_m} q_m \tag{5}$$

where $\hat{\delta}_{ele}^m$ is the aircraft model elevator deflection demand. The term $k_{q_m} q_m$ in equation (5) effectively acts as a damper, with k_{q_m} chosen experimentally such that any external perturbation is sufficiently damped out.

Using the control law defined in (5) and with $k_{q_m} = 0.1\,\mathrm{N\,m\,s/rad}$, the stability characteristics of the equilibria, in the regions covering both the inner and outer high α LCO, were studied using a total of eleven nominal elevator positions within $-21° \leq \hat{\delta}^m_{ele} \leq -12°$. This range of elevator positions is of interest because the aircraft pitch dynamics exhibit multiple solutions (equilibria and LCO), as previously discussed in Section 3.1 and shown in Figure 3. Results for two of these tests are presented in detail, namely for $\hat{\delta}^m_{ele} = -15°$ and $\hat{\delta}^m_{ele} = -17.5°$, followed by a discussion of all the tests.

Figure 4a shows the aircraft model 1-DOF pitch limit cycle suppression time histories and phase portraits for a nominal input of $\hat{\delta}^m_{ele} \approx -15°$. Subfigures 4ai to 4aiii show the time histories for the aircraft model elevator, pitch angle and pitch rate, respectively. Three sections are of interest: first with the controller off a pitch LCO can be observed in the region $1.4\,\mathrm{s} \leq t \leq 10\,\mathrm{s}$. The controller is switched on and the LCO is suppressed using the elevator in the region $10\,\mathrm{s} \leq t \leq 17.4\,\mathrm{s}$. Lastly, in the region $17.4\,\mathrm{s} \leq t \leq 26.4\,\mathrm{s}$ the controller is switched off and both the pitch angle and pitch rate start increasing until they reach the LCO, indicating that the equilibrium point is unstable.

Figures 4aiv to 4avi show the aircraft model pitch angle and pitch rate phase portraits for time segments $1.4\,\mathrm{s} \leq t \leq 8.4\,\mathrm{s}$, $13.4\,\mathrm{s} \leq t \leq 17.4\,\mathrm{s}$ and $17.4\,\mathrm{s} \leq t \leq 26.4\,\mathrm{s}$, respectively. A fully developed pitch LCO can be observed in Figure 4aiv, with the magnitudes of the pitch angle and pitch rate ranging over $12° \leq \theta_m \leq 25°$ and $-86\,°/\mathrm{s} \leq q_m \leq 76\,°/\mathrm{s}$, respectively. Figure 4avi shows the controller successfully suppressing the pitch LCO, and the aircraft maintaining its position at $\theta_m \approx 18.6°$. Figure 4avii, shows the controller switched off and the system returning to the pitch LCO, indicating that the equilibrium point is unstable.

In a similar fashion, Figure 4b shows the aircraft model 1-DOF pitch limit cycle suppression time histories and phase portraits for a nominal input of $\hat{\delta}^m_{ele} \approx -17.5°$. At the beginning of this test the controller is switched off and the nominal elevator deflection is held constant. Then a series of step inputs are commanded to the aircraft elevator to act as perturbations to the system. The characteristics of the first and last step inputs are $\Delta\delta^m_{ele} \approx 4°$ and $\Delta t \approx 0.3$ s and $\Delta\delta^m_{ele} \approx 4°$ and $\Delta t \approx 1.7$ s, respectively. The time histories for the aircraft model elevator, pitch angle and pitch rate are shown in Figures 4bi to 4biii.

With the controller switched off, both the pitch angle and pitch rate remain bounded around the equilibrium point indicating that the equilibrium point is stable, see Figures 4bii, 4biii and 4biv. Then at $t \approx 26$ s, an elevator step input acting as a perturbation is applied and the system oscillates around the equilibrium but the oscillation is damped down. Figure 4bv shows the corresponding phase plane representation for this perturbation and a small orbit can be seen, suggesting an inner LCO. Five additional step inputs are applied with similar results. From this, we conclude that this inner LCO is unstable.

At $t \approx 65$ s a step input with the same amplitude is applied over a larger duration and the system transitions to a stable outer pitch LCO. Figure 4bvi shows the aircraft model pitch angle and pitch rate phase portrait corresponding to this perturbation.

The results from this experiment suggest that in the region of $\theta_m \approx 20°$, the aircraft model has at least three solutions: a stable equilibrium point, a unstable inner LCO and a stable outer LCO.

Similar results were obtained for the remaining elevator nominal positions. An additional test was carried out in which a slow ramp input to the aircraft ele-

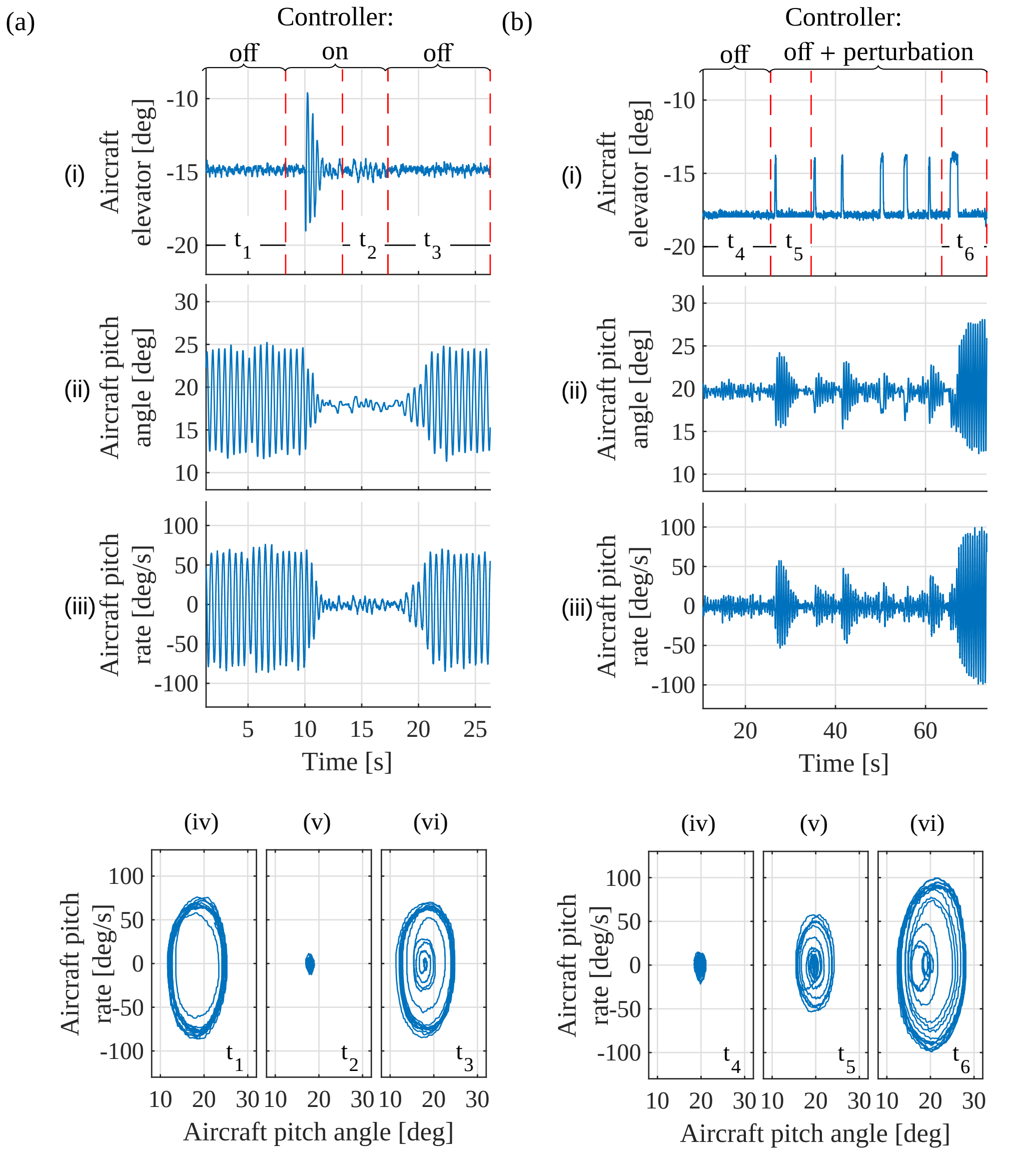

Figure 4: Aircraft model 1-DOF pitch limit cycle suppression time histories and phase portraits: (a) nominal input $\hat{\delta}^m_{ele} \approx -15°$ and (b) nominal input $\hat{\delta}^m_{ele} \approx -17.5°$.

vator was commanded while the LCO-suppressing controller was active. This test allowed the equilibrium points for different elevator deflections to be obtained experimentally. The data is presented in the form of a bifurcation diagram in Figure 5 using the aircraft elevator as the bifurcation parameter. The experimentally obtained equilibria are shown (red 'x' markers) along with manually computed stable equilibria (solid black line) and unstable equilibria (dashed black line). It can be observed that the controller successfully tracked the equilibria, except for the region $\theta_m \approx 16°$. The equilibrium points are unstable in two regions: $-4° \leq \delta_{ele}^m \leq 0°$ and $-17° \leq \delta_{ele}^m \leq -11°$. Around these regions pitch LCO have been found. In the region $-22° \leq \delta_{ele}^m \leq -12°$, the stable LCO (black line with '+' markers) can be seen in Figure 5. Lastly, in the region $-19° \leq \delta_{ele}^m \leq -16°$, the unstable LCO is shown as a dashed black line with '+' markers. Note that these unstable LCO represent the boundary that separates the equilibria from the stable LCO, i.e. the separatrix of the system.

The results presented in this section show that the controller successfully suppressed the LCO behaviour in the 1-DOF aircraft model pitch experiment. The all-moving tailplane was able to provide the necessary control power to achieve this (the flow over the tailplane is not stalled in this high angle-of-attack region). By virtue of this technique, the stability characteristics of the aircraft's equilibria and LCO were determined and the inner unstable LCO has been identified for this model for the first time. From a fluid dynamics point of view, the causes behind the observed LCO behaviour are not entirely understood but it is possible that two flow breakdown structures are involved at high angle of attack, in a similar vein to the variation in lift hysteresis for the delta wing model in [20]: PIV experiments in a water tunnel tests suggested this behaviour was related to a dual-core

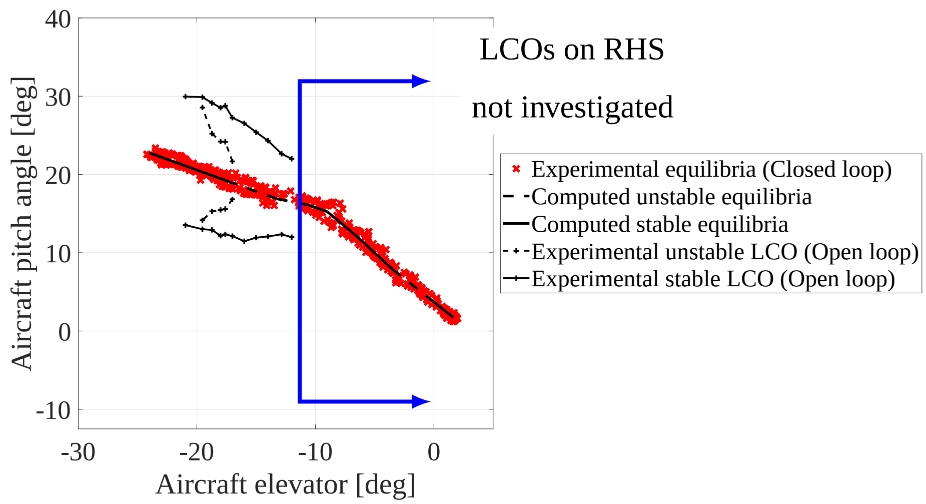

Figure 5: 1-DOF aircraft model pitch experimental bifurcation diagram.

leading-edge vortex phenomenon.

Whilst the application here is the sub-scale approximate Hawk aircraft model, the technique can be applied to any wind tunnel model which has actuated control effectors, thus enabling similar studies of stability and associated dynamical structure to be revealed experimentally. The approach can be extended to exploit the potential of 'control-based continuation': a technique for tracking the solutions and bifurcations of nonlinear experiments. It aims to achieve the equivalent of numerical continuation but applied to a physical experiment, through the use of 'minimally invasive' feedback control schemes – see [48] for an explanation of the method and [49] for an example of an application to wing aeroelastic responses in a wind tunnel. A simplified implementation of this technique on the Hawk model mounted on the manoeuvre rig has revealed additional complexity in its hysteretic behaviour [41].

4. Robustness of LCOs to Additional DOFs

Releasing additional degrees of freedom in the manoeuvre rig allows for the study of interaction of longitudinal phenomena, such as the limit cycles and hysteresis discussed in the previous section, with lateral-directional dynamics. This is especially important at higher angles of attack where effects of nonlinearity typically become relevant and asymmetric responses to symmetric conditions can occur: it is frequently the case that the development of stall in an aircraft results in roll and/or yaw when no lateral-directional inputs are given.

Here, to explore the interaction of the Hawk longitudinal LCO behaviour with its lateral-directional dynamics and its evolution as different degrees of freedom are freed up, a series of multi-DOF tests was performed. Using different combinations of model pitch, model yaw, model roll, arm roll and arm yaw degrees of freedom as appropriate, inputs to the Hawk model elevator, rudder and ailerons were used to drive the motion of the model. These experimental results are presented in three parts: firstly a 2-DOF configuration using the aircraft pitch and yaw DOF is presented, secondly two further 2-DOF configurations, one using the aircraft model pitch and roll DOF and another using the aircraft model pitch and arm roll DOF are considered; finally a 4-DOF (no heave) configuration is tested where compensation of roll motion using the aerodynamic compensator is used to keep the model gimbal roll angle as close as possible to zero.

4.1. 2-DOF Aircraft Pitch & Yaw

For the 2-DOF aircraft pitch and aircraft yaw experiments, five different constant inputs to the aircraft elevator were applied, namely $\delta^m_{ele} = [-2, -5, -10, -15, -20]°$, with a slow ramp applied to the aircraft rudder over the range $-39° \leq \delta^m_{rudd} \leq 39°$.

Using the time history data from this experiment, 2-DOF bifurcation diagrams were obtained following the procedure described in Section 3.1. The aircraft rudder was used as the bifurcation parameter and each aircraft elevator input setting was treated as an independent data set. The diagrams for $\delta^m_{ele} = [-2°, -5°, -10°, -15°, -20°]$, are shown in Figures 6a to 6e, respectively. The blue line represents a sweep of decreasing aircraft rudder δ^m_{rdd}, while the red line represents an increasing one. The black dashed lines represent the system's approximate equilibria. These were computed by taking an average of the values corresponding to the decreasing aircraft rudder δ^m_{rdd} sweep in each case, represented by the blue lines.

The analysis of the nonlinear phenomena for this experiment is divided into two: the low and high α LCO regions. The 2-DOF bifurcation diagrams for the first region are shown in Figures 6a and 6b. These show that the low α LCO persists throughout the range of tested ψ_m (unlike in the tests with different *model* yaw angles – not shown here [35]). Figure 6b shows a small amplitude oscillation in yaw angle for $3° \leq \delta^m_{rudd} \leq 27°$. This suggests that the shadowing of the horizontal tail by the wing/fuselage, proposed in Section 3.1 as the cause of the low angle-of-attack LCO, may also affect the fin in this region, indicating a lack of symmetry. Figures 6c, 6d and 6e coincide with the high α LCO region. In contrast with the low α LCO region, strong interaction between the pitch and yaw dynamics can be observed. This interaction can be better observed in Figure 6f which shows a phase portrait for $\delta^m_{ele} = -15°$, $-6° \leq \delta^m_{rudd} \leq 3°$. This phase portrait was produced using data from the segment between the vertical dashed lines in Figure 6d. The time history for this region shows that the number of orbits of the LCO pitch component is twice that of the LCO yaw component which indicates that the pitch component has double the frequency of the yawing motion.

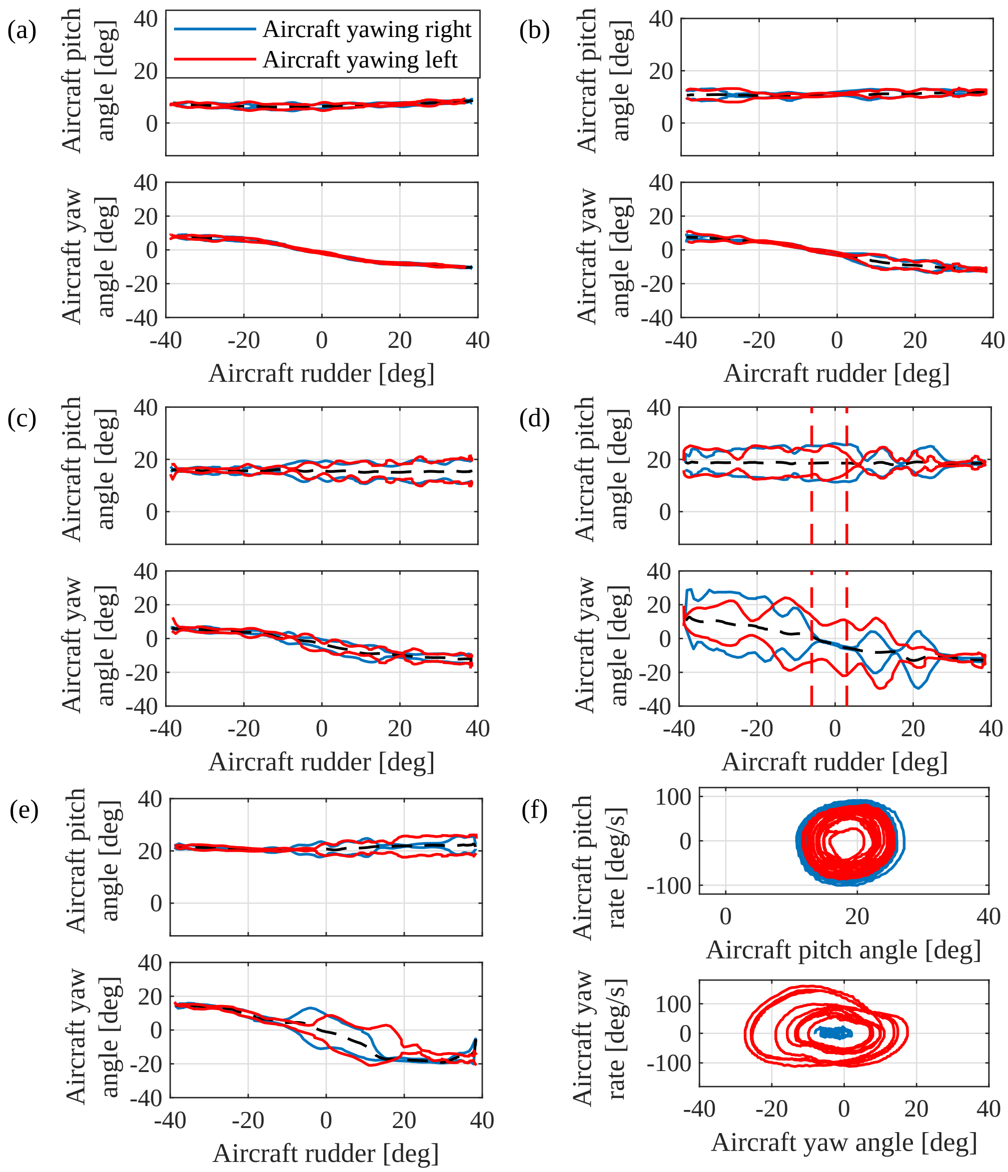

Figure 6: 2-DOF aircraft model pitch & yaw experimental bifurcation diagrams for: (a) $\delta^m_{ele} = -2°$, (b) $\delta^m_{ele} = -5°$, (c) $\delta^m_{ele} = -10°$, (d) $\delta^m_{ele} = -15°$, (e) $\delta^m_{ele} = -20°$ and (f) phase portrait for $\delta^m_{ele} = -15°$ and $-6° \leq \delta^m_{rudd} \leq 3°$.

4.2. 2-DOF Aircraft Pitch & Roll

A series of 2-DOF aircraft roll and pitch experiments was carried out to study coupled pitch-roll interaction in the regions where LCO behaviour appears. Two configurations were studied, one encompassing the aircraft roll and pitch DOFs and a second one using the aircraft pitch and the arm roll DOFs.

4.2.1. 2-DOF Aircraft Pitch & Aircraft Roll

In this experiment a slow ramp-and-hold input to the aircraft elevator was applied and the aircraft roll and pitch motion responses were recorded. It was found that at $\theta_m \approx 15°$, the roll-pitch interaction caused the aircraft to reach the physical limits of the roll gimbal (approximately $\pm 38°$). As a consequence a reduced range of pitch motions is presented here.

Figure 7a shows the time histories for this experiment, with the aircraft model elevator deflection, roll angle, pitch angle, roll rate and pitch rate shown in Figures 7ai to 7av, respectively. Note that the range of elevator input is less here than in Section 3.1 due to the roll gimbal mechanical limits being reached at more negative elevator settings. In this Figure a pitch LCO at low α can be seen in the regions $35\,\mathrm{s} \leq t \leq 75\,\mathrm{s}$ and $340\,\mathrm{s} \leq t \leq 380\,\mathrm{s}$, with a maximum rate of $54\,°/\mathrm{s}$. In the region $150\,\mathrm{s} < t < 230\,\mathrm{s}$, it can be observed that the aircraft experiences roll oscillations and reaches the roll gimbal limits. When the aircraft elevator angle starts increasing at $t \approx 250\,\mathrm{s}$, the roll oscillations begin to damp down and the aircraft roll angle goes back to a steady state bounded by $-10° < \phi_m < 10°$.

The point at which the low-α LCO appears, at $t \approx 35\,\mathrm{s}$, and disappears, at $t \approx 380\,\mathrm{s}$, is at a higher pitch amplitude than in the 1-DOF case and is accompanied by an offset in average roll angle. This negative roll angle persists through the LCO and after exiting the LCO at higher α, i.e. a roll asymmetry exists for all pitch angles above approx. $\approx 5°$. Its existence appears to be linked to the bifurcation giving rise to the LCO, with zero roll angle at lower angles of attack (before the tailplane becomes immersed in the wing-fuselage wake) and a roll offset when it is immersed and when it emerges below the wake at higher α.

Figure 7b shows a smoothed experimental 2-DOF bifurcation diagram obtained following the procedure described in Section 3.1 by excluding the data points that correspond to motions where the aircraft reaches its roll gimbal limits. In this diagram the aircraft elevator is the bifurcation parameter. In Figure 7bii the 'jump' in roll angle that was observed in Figure 7a (at the Hopf bifurcation point at which the low-α LCO is borne) is evident – at $\delta_{ele}^{m} \approx 1°$ when the aircraft model is pitching up and $\delta_{ele}^{m} \approx 2°$ when pitching down. The roll angle is then more constant at pitch angles above the low α LCO (observed in Figure 7bi in the region $-2° \leq \delta_{ele}^{m} \leq 3°$), although there are changes in value at higher α.

Figure 7c shows a detailed view of the time histories for $246\,\mathrm{s} \leq t \leq 254\,\mathrm{s}$. Roll oscillations can be observed while the elevator deflection is held constant, which suggest there may exist periodic solutions in this region. Using the data shown in Figure 7c, a phase portrait diagram was constructed (see Figure 7d). While the phase portrait shows almost no excitation of the aircraft pitch dynamics, several orbits can be observed in the roll motion plot, suggesting the possibility that roll oscillations may drive the onset of the pitch oscillations observed when the gimbal roll DOF was locked.

The results from this experiment confirm the existence of roll-pitch interaction. They suggest that the roll oscillation may delay the onset of pitch oscillations to higher α, although the fact that the roll motion hits the gimbal limits makes it difficult to reach definite conclusions in this respect.

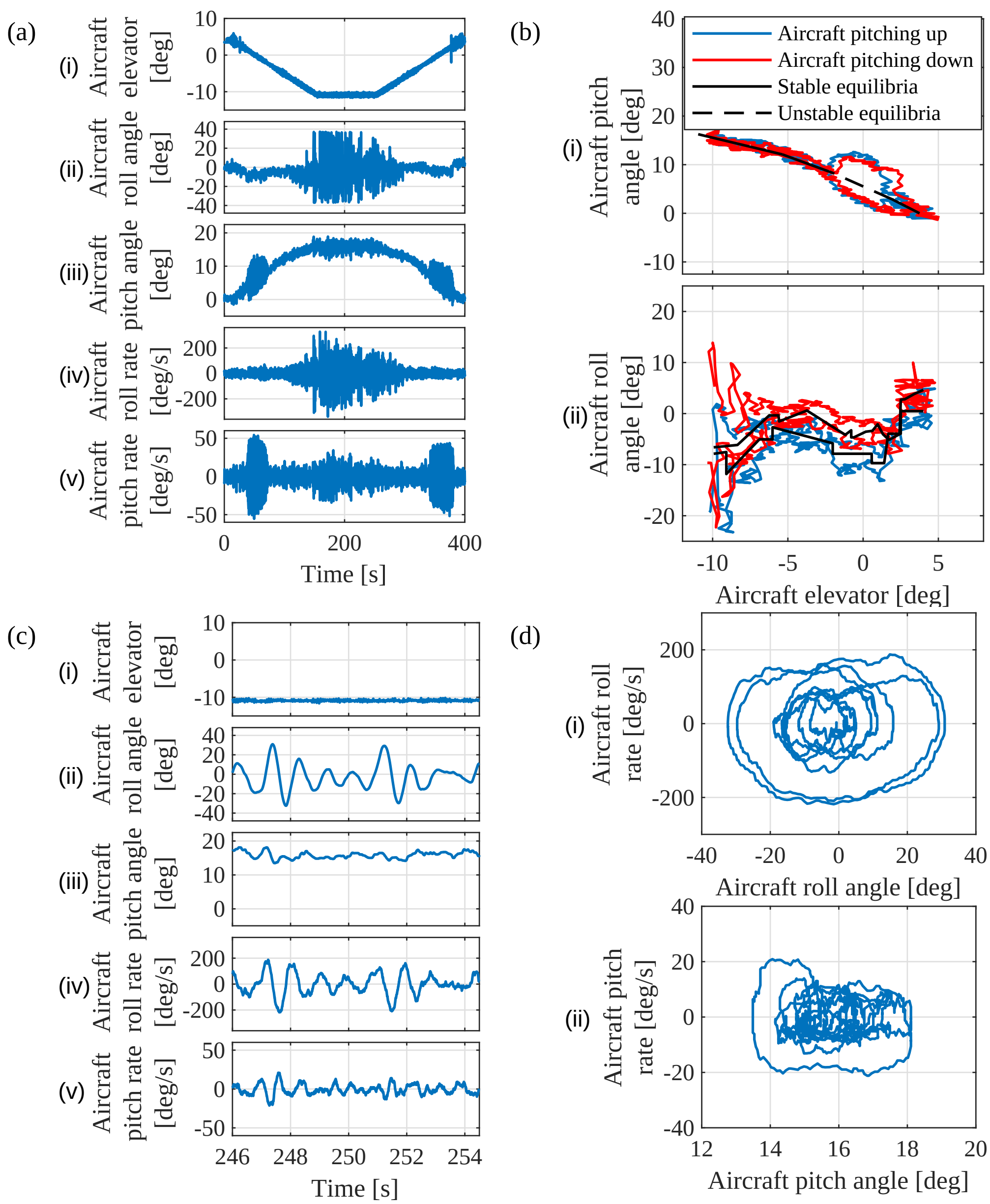

Figure 7: 2-DOF aircraft model roll and pitch experiment: (a) time histories, (b) bifurcation diagram, (c) time histories detailed view and (d) phase portrait diagram.

4.2.2. 2-DOF Aircraft Pitch & Arm Roll

Whilst the above results highlight the potential benefit of adding a roll DOF, i.e. to explore longitudinal-lateral interaction, they also demonstrated the limitation of relying on an aircraft-mounted gimbal with angular constraints. Here, a 2-DOF aircraft pitch and roll experiment was carried out in similar fashion to the one presented in the previous subsection except that roll was obtained through the arm gimbal roll rather than the model gimbal: the arm gimbal allows unlimited motion. A slow ramp input to the aircraft elevator was applied and the aircraft pitch and arm roll motion responses were recorded.

To account for the offset between the Hawk model CG and the arm gimbal roll axis, the aircraft roll motion was computed using an extended Kalman filter (EKF) applied to signals from the IMU mounted on the aircraft model. Note that the influence of this offset is assumed to be negligible when considering rig heave and sway as it is very small (approx. 14 mm).

Figures 8ai, to 8av show the time histories of the aircraft model elevator deflection, the aircraft roll angle, pitch angle, roll rate and pitch rate, respectively. Two LCO can be observed at low and high α in the regions $65\,\mathrm{s} \leq t \leq 130\,\mathrm{s}$, $680\,\mathrm{s} \leq t \leq 760\,\mathrm{s}$, $200\,\mathrm{s} \leq t \leq 330\,\mathrm{s}$ and $500\,\mathrm{s} \leq t \leq 620\,\mathrm{s}$, respectively. This is consistent with the experimental results presented in Sections 3 and 4.1, except that the onset of the high α LCO is delayed to a higher angle of attack (approx. 20°). These LCO are easier to study using the 2-DOF arm roll and aircraft pitch smoothed bifurcation diagram shown in Figure 8b. The bifurcation diagram was obtained using the same data processing method as described in Section 3.1 and using the aircraft elevator as the bifurcation parameter.

The low and high α LCO can be observed in Figure 8bi in the regions $-3° \leq \delta^m_{ele} \leq 3°$

and $-9.5° \leq \delta_{ele}^{m} \leq -23°$, respectively. In Figure 8bii, it can be observed that the roll angle decreases proportionally with the aircraft elevator in the regions $3° < \delta_{ele}^{m} < 10°$ and $-9° < \delta_{ele}^{m} < -3°$, suggesting lateral dynamics asymmetry. This behaviour is similar to that observed in the aircraft pitch configuration presented in Section 4.2.1. The roll angle does appear to vary more smoothly between these two regions, which coincides with the onset of the low α LCO, without the discrete 'jump' evident in Figure 7b.

The high α LCO is preceded by oscillations in roll in the region delimited by $-12° < \delta_{ele}^{m} < -9°$, suggesting that roll oscillations may induce the onset of pitch oscillations. It is also noticeable that there is an increase in roll angle amplitude when the LCO dies out at higher α ($\delta_{ele}^{m} < -21°$).

When compared with the 1-DOF aircraft pitch experiment two points are worth noting. Firstly, the low α LCO seems to be completely driven by longitudinal effects. Secondly, the roll-pitch interaction in the high α LCO is strong enough to change the shape of the hysteretic behaviour region (around $\delta_{ele}^{m} = -10°$ to $-12°$), almost to the point of making it disappear. This suggests that, in this region, the onset of the pitch oscillations may be induced by the roll dynamics.

The results from this experiment indicate that there is strong roll-pitch interaction throughout the test space. This interaction is observed in the form of arm roll deflection. Given the inertia and pendulum effect of the arm, this arm roll deflection suggests the existence of significant rolling moments induced by the aircraft on the rig arm. Clearly, this configuration has the disadvantage of the aircraft model dynamic response being modified by the effects of arm inertia and the offset of the rig CG from the roll axis. Whilst this can be accounted for in processing results, it does preclude correct physical simulation of an aircraft model

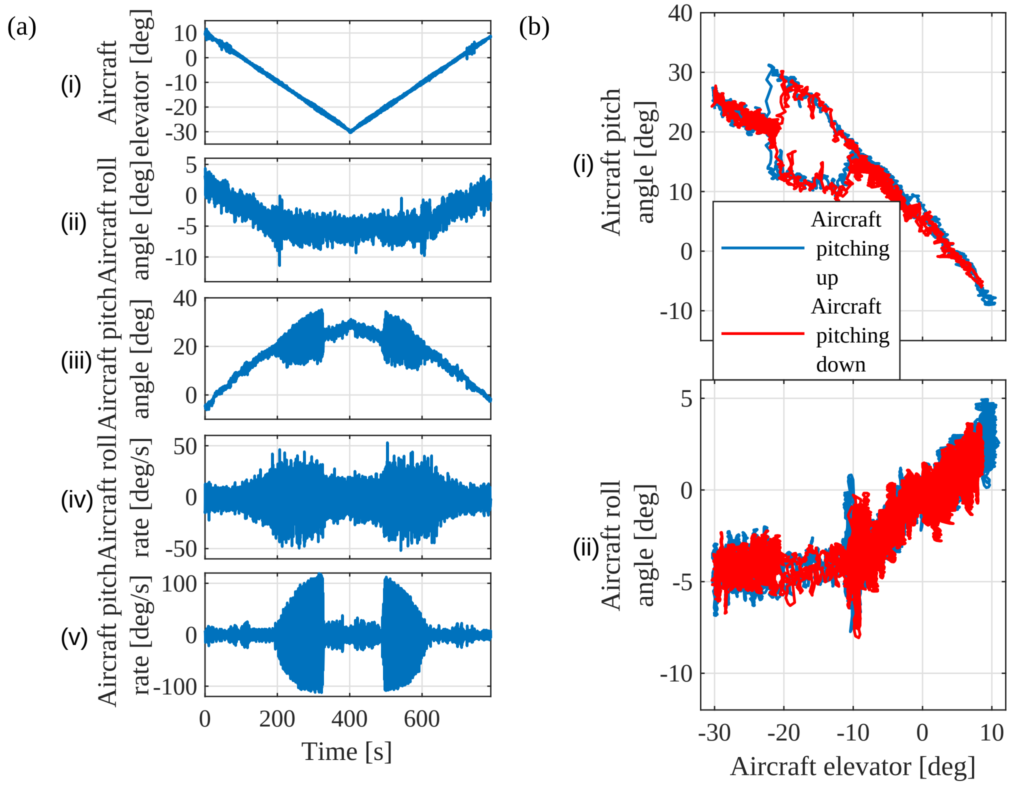

Figure 8: 2-DOF arm roll and aircraft pitch experiment: (a) time histories and (b) bifurcation diagram.

that has no constraints on motion in its degrees of freedom. On the other hand, when testing under the approximate free-to-roll conditions afforded by the model gimbal roll DOF, the envelope within which physical simulation could be carried out is constrained by the roll gimbal limits (as seen in Section 4.2.1). In the case of the Hawk model, if it were free to roll without gimbal limits and without rig inertial effects, it is likely that the roll-pitch interaction would lead to more complex behaviour such as wing rock and/or wing drop. Therefore, in the next section, we exploit the rig compensator to attempt to eliminate the influence of the rig arm on the model roll dynamics.

5. Compensation of Rig Dynamics

A 4-DOF experiment was carried out to study the open loop behaviour of the aircraft model in a multi-DOF configuration where only the arm gimbal pitch DOF was locked, such that the aircraft is unable to heave. It is however able to pitch, yaw, roll (both via the aircraft and the arm gimbals) and sway. In this experiment, a flight control stick was used to manually control the aircraft ailerons and elevator. The rig arm roll motion was controlled via the aerodynamic control surfaces on the compensator (referred to as compensator ailerons), using a control law with feedback of model roll rate and roll angle relative to the arm. The control objective was to track the aircraft's roll motion, keeping the model gimbal roll angle as close as possible to zero. Here, the model gimbal roll DOF, with its low inertial load, can be thought of as allowing for fast aircraft roll dynamics while the arm roll DOF allows slow dynamics over the full 360° range.

Figure 9 shows the aircraft model motion time histories, with panels ai to aiii showing the control inputs and the rest the aircraft model motion variables. The control inputs consist of:

- compensator aileron deflection (actively controlled), δ^c_{ail}, Figure 9ai,
- aircraft model aileron deflection, δ^m_{ail}, Figure 9aii and
- aircraft model elevator deflection, δ^m_{ele}, Figure 9aiii.

The aircraft model motion variables are:

- roll rate, p_m, Figure 9aiv,
- pitch rate, q_m, Figure 9av,
- yaw rate, r_m, Figure 9avi,
- angle of attack, α_m (blue solid line), and pitch angle, θ_m (red dashed line), shown in Figure 9avii,
- angle of sideslip, β_m (blue solid line), and yaw angle, ψ_m (red dashed line), shown in Figure 9aviii,
- roll angle, ϕ_m, shown in Figure 9aix and
- aircraft gimbal roll angle, ϕ_g, shown in Figure 9ax.

Figure 9b shows a magnification of 9a. The aircraft angles of attack and sideslip were computed off-line using the arm gimbal angles, the model gimbal angles and the aircraft rotational rates. The equations used to compute these can be found in Araujo-Estrada [35].

With the aircraft in an initial trimmed state, the aircraft elevator is slowly decreased to increase the aircraft angle of attack (see Figures 9aiii and 9avii). Two segments are of interest. Firstly, in the region $2\,\mathrm{s} \leq t \leq 15\,\mathrm{s}$, the low α pitch LCO previously identified can be observed (Figures 9av and 9avii). In keeping with the previous 2-DOF tests (Section 4), there seems to be little interaction between the aircraft pitch motion and the remaining DOFs, for which time histories show relatively small magnitude changes.

Secondly, more complex behaviour involving all the DOFs can be observed in the region $19\,\mathrm{s} \leq t \leq 30\,\mathrm{s}$. At $t \approx 19\,\mathrm{s}$, an increase in the rolling moment and side force is experienced by the aircraft (manifested via the ψ_m and ϕ_m time histories in Figures 9aviii and 9aix). A manual input to δ^m_{ail} is applied to correct ϕ_m (Figure 9aii). After this, δ^m_{ele} is decreased further and the system seems to track the equilibria. At $t \approx 25\,\mathrm{s}$, the aircraft accelerates in roll ϕ_m causing a fast change in the gimbal roll angle ϕ_g. This rapid change in the dynamics is easier to observe in Figures 9bix and 9bx. As a consequence, the compensator ailerons deflect (Figure 9bi), allowing $|\phi_m| > 100°$ (Figure 9bix), without reaching the gimbal physical limits (Figure 9bx). At $t \approx 26.8\,\mathrm{s}$, the aircraft accelerates once more in roll and a sharp change in ϕ_g is observed. The compensator ailerons deflect to compensate the roll motion, allowing the aircraft to complete two roll revolutions (Figures 9ai and 9aix), before the aircraft ultimately reaches the gimbal mechanical limits (Figure 9bx). Finally, the aircraft aileron and elevator stick inputs are released, and the system returns to a trimmed state.

The results from this experiment confirm that there is negligible interaction between the aircraft pitch motion and the other DOFs in the low α LCO. Also, in the region corresponding to the previously identified high α LCO, complex behaviour involving all DOF is observed and the motion response is dominated by the lateral-directional dynamics. Further insight into the roll asymmetries respon-

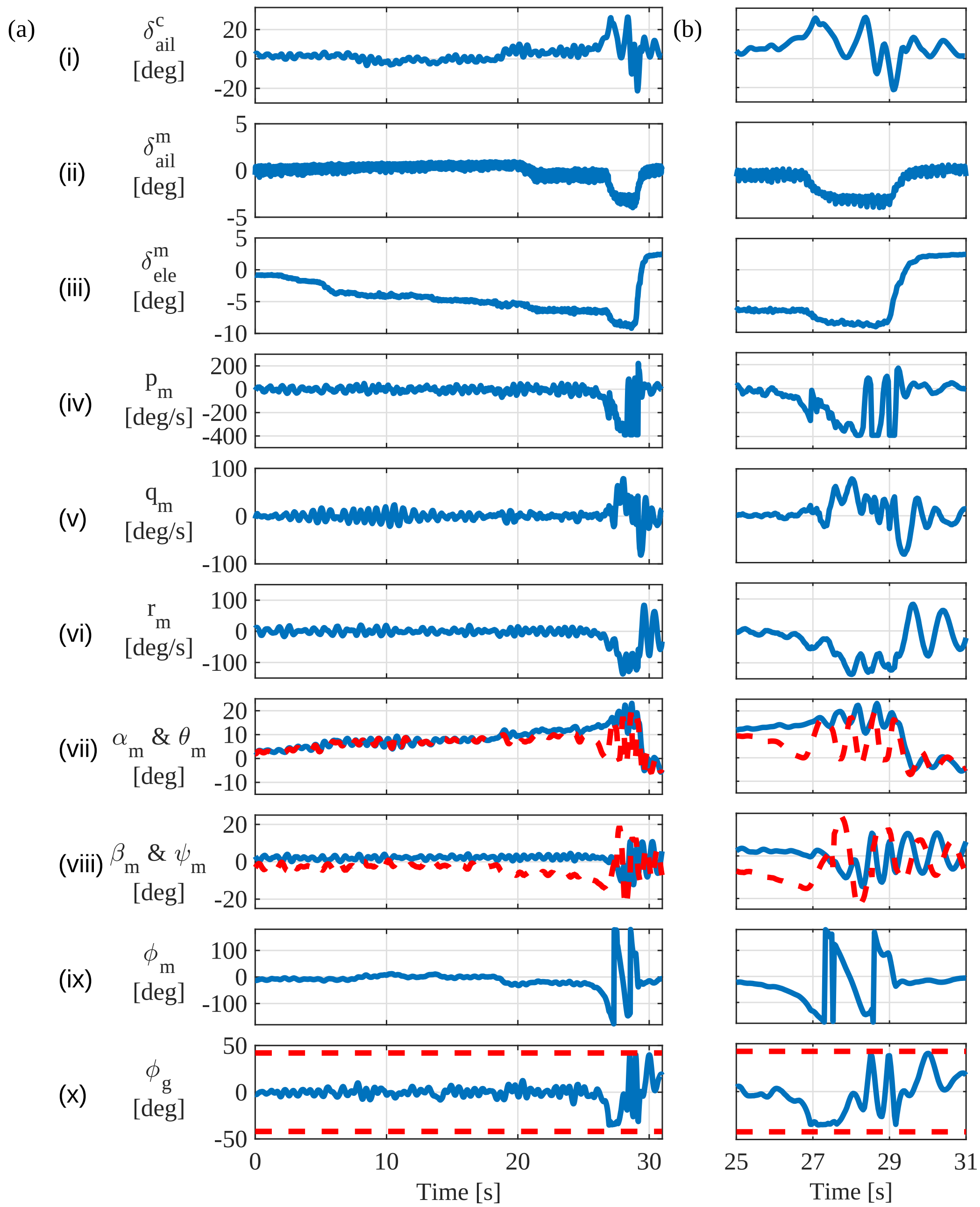

Figure 9: 5-DOF No-heave: (a) aircraft motion time histories and (b) time histories detailed view. Where two lines are plotted, the first listed in the label is plotted as a solid line.

sible for the onset of the high-α LCO has been developed in a separate study of the Hawk model equilibria, using a ‘minimally invasive’ feedback controller, in a different multi-DOF test [41]. Lastly by controlling the arm roll via the compensator the allowable model roll was increased substantially before the roll rate results in stops being reached.

This 4-DOF test demonstrates the added capability of arm roll tracking compensation in revealing coupled responses of an aircraft model. A complementary compensation strategy, proposed by Navaratna et. al [38], utilizes a load cell incorporated in the rig just below the model gimbal and aims to reduce the influence of the arm dynamics on the aircraft model motions by feeding back the reaction force between the aircraft and the rig arm to the aerodynamic compensator. Simulation results indicate that by using this approach, the aircraft model dynamics does more closely match equivalent free flight behaviour for various modes of motion.

6. Concluding Remarks

In this paper, the potential of gaining new insights into aircraft behaviour using novel wind tunnel manoeuvre rigs is examined. Possible testing regimes are discussed and, using an approximate BAe Hawk wind tunnel model, example results and associated insights are presented. Specifically, for the Hawk model, both open and closed loop tests are used to reveal nonlinear behaviour, which manifests itself as LCO and were observed in all testing configurations.

By releasing the manoeuvre rig DOFs incrementally in open loop experiments it was possible to observe the evolution of complex dynamic behaviour. First, a 1-DOF pitch test allowed two main regions where pitch LCO appear to be identified:

one around $\theta = 5°$ (low α) and another starting at $\theta = 15°$ (high α). These results are in agreement with those previously presented by Kyle [42], Davison [43] and Pattinson [34]. Additionally, the LCO structure was found to be more complex than previous tests had suggested, with evidence of an inner LCO within the high α LCO region. Application of a feedback controller in a 1-DOF model pitch configuration allowed the stability characteristics of the model equilibria and LCO to be assessed and allowed the inner unstable LCO within the high α LCO to be identified.

When a 2-DOF aircraft pitch and yaw configuration was used it was found that the low α LCO was dominated by pitch motions. The high α LCO region is more complex: both pitch and yaw motions are present with the pitch component having twice the frequency of the yaw component. A strong roll-pitch interaction in the high α LCO was identified using 2-DOF results from both the aircraft roll and pitch and the aircraft pitch and arm roll. As a result of the high roll rates induced by this coupling, limitations arising from motions exceeding gimbal mechanical limits were evident in the case where the model roll gimbal was used. When the arm roll DOF was deployed instead, revealing the magnitude of the rolling moment being exerted by the aircraft model on the arm, the impact of arm inertia and offset CG on the model responses was also highlighted. These roll motion issues justified the deployment of the rig compensator surfaces in order to allow unconstrained model roll motions whilst minimizing rig effects. This was demonstrated in the last of the experiments reported in the paper, in which feedback control to the compensator ailerons was implemented in a 4-DOF (roll-pitch-yaw-sway) configuration. This confirmed the strong roll-pitch coupling characteristics and allowed the roll testing envelope to increase. However, the model did ultimately reach its gimbal mechanical limits, thus indicating that the aircraft roll dynamics are faster than that of the rig arm so that compensation was not fully achieved in this case.

For the Hawk model, the experimental results presented here provide a new perspective on the nature of what was previously considered to be a pitch-only LCO in the high α region, shedding light on the interaction between the longitudinal and lateral-directional dynamics where the LCO appears.

More generally, the experiments reported in this paper reveal the capacity of this novel type of wind tunnel dynamic test rig to physically simulate the motions of an air vehicle in multiple degrees of freedom, and to use open- and closed-loop testing to reveal insights into the responses arising from nonlinear and unsteady aerodynamic effects, including evaluation of stability and hysteresis phenomena. The nature of this type of rig, where the aircraft model motion is driven by its own control surfaces, is seen to be particularly well suited to studies of complex or counter-intuitive behaviours such as in the initiation of aircraft upset/loss-of-control scenarios. Future application of this technique could be used for evaluating additional types of nonlinear phenomena such as aerodynamic hysteresis, for enhanced flight characteristics modelling and for designing and evaluating flight control laws. For flight characteristics modelling, the rig – which has recently benefitted from the addition of a load cell to measure forces and moments between the model and the rig arm - can be used along with traditional/standard modelling approaches to extract stability derivatives in combination with Machine Learning methods [39], to validate longitudinal stability derivatives estimates of novel aircraft in subsonic regimes obtained via CFD simulations [40], to develop and evaluate online system identification techniques to obtain aerodynamic parameters of fixed-wing aircraft in upset conditions like stall [50], as well as to improve understanding of flexible aircraft flight dynamics [51] and possibly also novel concepts such as flapping-wing MAVs [52, 53] and vectored thrust urban air mobility concepts, also known as Personal Aerial Transportation Systems (PATS) [54]. Alternatively, new techniques (like the one presented here), can be used to build experimental bifurcation diagrams and model the dynamical structure of the aircraft. In terms of flight control law development, the rig can be used to design and evaluate controllers based on established classic and model-based approaches (realising DOFs one at a time and modifying the controller's gains appropriately) or to test novel Machine Learning-based controllers, such as attitude controllers for fixed-wing UAVs [55, 56].

Acknowledgments

S. A. Araujo-Estrada's research was supported by the Science and Technology National Council (CONACYT-Mexico), studentship # 215262. S. Neild was supported by an EPSRC fellowship (EP/K005375/1). The authors thank Prof. Mikhail Goman for his insights and suggestions in support of the development of this rig and the work described in this paper. The authors would like to thank and acknowledge Mr Lee Winter from the University of Bristol wind tunnel laboratory, for his invaluable support and work during the refitting, assembly and modification of the equipment used to carry out the experiments presented in this paper.

References

[1] E. Relf, T. Lavender, A Continuous Rotation Balance for the Measurement of L_p at Small Rates of Roll, Tech. rep., Aeronautical Research Committee (ARC), Reports & Memoranda No. 828 (1922).

[2] T. Lavender, A Continuous Rotation Balance for the Measurement of Pitching and Yawing Moments Due to Angular Velocity of Roll (M_p and N_p), Tech. rep., Aeronautical Research Committee (ARC), Reports & Memoranda No. 936 (1925).

[3] J. D. Nicolaides, R. S. Eikenberry, Dynamic Wind Tunnel Testing Techniques, in: AIAA Aerodynamic Testing Conference, American Institute of Aeronautics and Astronautics (AIAA), Los Angeles, Califormia, 1966. doi:10.2514/6.1966-752.

[4] K. Orlik-Ruckemann, Review of Techniques for Determination of Dynamic Stability Parameters in Wind Tunnels, in: Dynamic Stability Parameters, Lecture Series, LS-114, Advisory Group for Aerospace Research and Development (AGARD), Moffett Field, California, 1981.

[5] M. Huang, Z. W. Wang, A review of wind tunnel based virtual flight testing techniques for evaluation of flight control systems, International Journal of Aerospace Engineering 2015 (1) (2015) 1–22. doi:10.1155/2015/672423.

[6] J. M. Brandon, J. V. Foster, Recent dynamic measurements and considerations for aerodynamic modeling of fighter airplane configurations, in: 23rd

Atmospheric Flight Mechanics Conference, American Institute of Aeronautics and Astronautics Inc, AIAA, Boston, Massachusetts, 1998, pp. 633–649. doi:10.2514/6.1998-4447.

[7] P. C. Murphy, V. Klein, Estimation of aircraft unsteady aerodynamic parameters from dynamic wind tunnel testing, in: AIAA Atmospheric Flight Mechanics Conference and Exhibit, Montreal, Canada, 2001. doi:10.2514/6.2001-4016.

[8] G. H. Shah, K. Cunningham, J. V. Foster, C. M. Fremaux, E. C. Stewart, J. E. Wilborn, W. Gato, D. W. Pratt, Wind-Tunnel Investigation of Commercial Transport Aircraft Aerodynamics at Extreme Flight Conditions, in: World Aviation Congress & Exposition, SAE International, Phoenix, Arizona, 2002. doi:10.4271/2002-01-2912.

[9] K. Cunningham, J. V. Foster, G. H. Shah, E. C. Stewart, R. A. Rivers, J. E. Wilborn, W. Gato, Simulation Study of a Commercial Transport Airplane During Stall and Post-Stall Flight, in: World Aviation Congress & Exposition, SAE International, 2004. doi:10.4271/2004-01-3100.

[10] T. Jordan, W. Langford, C. Belcastro, J. Foster, G. Shah, G. Howland, R. Kidd, Development of a Dynamically Scaled Generic Transport Model Testbed for Flight Research Experiments, Tech. rep., National Aeronautics and Space Administration (jan 2004).

[11] T. D. Rawlins, High-incidence stabilator as an out-of-control recovery device for a fixed-wing subscale transport unmanned air vehicle, in: 43rd AIAA

Aerospace Sciences Meeting and Exhibit, Reno, Nevada, 2005, pp. 3821–3851. doi:10.2514/6.2005-1022.

[12] J. V. Foster, K. Cunningham, C. M. Fremaux, G. H. Shah, E. C. Stewart, R. A. Rivers, J. E. Wilborn, W. Gato, Dynamics modeling and simulation of large transport airplanes in upset conditions, in: AIAA Guidance, Navigation, and Control Conference and Exhibit, Vol. 2, American Institute of Aeronautics and Astronautics, San Francisco, California, 2005, pp. 826–838. doi:10.2514/6.2005-5933.

[13] K. Cunningham, J. V. Foster, G. H. Shah, E. C. Stewart, R. N. Ventura, R. A. Rivers, J. E. Wilborn, W. Gato, Simulation study of flap effects on a commercial transport airplane in upset conditions, in: AIAA Atmospheric Flight Mechanics Conference and Exhibit, San Francisco, California, 2005, pp. 373–386. doi:10.2514/6.2005-5908.

[14] A. M. Murch, J. V. Foster, Recent NASA research on aerodynamic modeling of post-stall and spin dynamics of large transport airplanes, in: 45th AIAA Aerospace Sciences Meeting, American Institute of Aeronautics and Astronautics Inc., Reno, Nevada, 2007, pp. 5553–5572. doi:10.2514/6.2007-463.

[15] P. C. Murphy, V. Klein, Transport aircraft system identification from wind tunnel data, in: AIAA Atmospheric Flight Mechanics Conference and Exhibit, American Institute of Aeronautics and Astronautics Inc., Honolulu, Hawaii, 2008. doi:10.2514/6.2008-6202.

[16] P. C. Murphy, V. Klein, Transport aircraft system identification us-

ing roll and yaw oscillatory wind tunnel data, in: AIAA Atmospheric Flight Mechanics Conference 2010, AIAA, Ontario, Canada, 2010. doi:10.2514/6.2010-8122.

[17] B. Owens, J. Brandon, M. Croom, M. Fremaux, G. Heim, D. Vicroy, Overview of Dynamic Test Techniques for Flight Dynamics Research at NASA LaRC, in: 25th AIAA Aerodynamic Measurement Technology and Ground Testing Conference, American Institute of Aeronautics and Astronautics (AIAA), San Francisco, California, 2006. doi:10.2514/6.2006-3146.

[18] R. M. Cummings, S. A. Morton, S. G. Siegel, Numerical prediction and wind tunnel experiment for a pitching unmanned combat air vehicle, Aerospace Science and Technology 12 (5) (2008) 355–364. doi:10.1016/J.AST.2007.08.007.

[19] D. I. Ignatyev, A. N. Khrabrov, A. I. Kortukova, D. A. Alieva, M. E. Sidoryuk, S. G. Bazhenov, Interplay of unsteady aerodynamics and flight dynamics of transport aircraft in icing conditions, Aerospace Science and Technology 104 (2020) 105914. doi:10.1016/j.ast.2020.105914.

[20] Y. Yi, T. Hu, P. Liu, Q. Qu, G. Eitelberg, R. A. Akkermans, Dynamic lift characteristics of nonslender delta wing in large-amplitude-pitching, Aerospace Science and Technology 105 (2020) 105937. doi:10.1016/j.ast.2020.105937.

[21] M. Rein, G. Höhler, A. Schütte, A. Bergmann, T. Löser, Ground-based simulation of complex maneuvers of a delta-wing aircraft, in: 25th AIAA Aero-

dynamic Measurement Technology and Ground Testing Conference, San Francisco, California, 2006, pp. 418–424. doi:10.2514/6.2006-3149.

[22] M. Rein, G. Höhler, A. Schütte, A. Bergmann, T. Löser, Ground-based simulation of complex maneuvers of a delta-wing aircraft, Journal of Aircraft 45 (1) (2008) 286–291. doi:10.2514/1.30033.

[23] T. Loeser, A. Bergmann, Capabilities of Deployment Tests at DNW-NWB, in: Fluid Dynamics of Personnel and Equipment Precision Delivery from Military Platforms, Neuilly-sur-Seine, France, 2006, pp. 10–1 – 10–12.

[24] T. D. Loeser, D. D. Vicroy, A. Schütte, SACCON static wind tunnel tests at DNW-NWB and $14' \times 22'$ NASA LaRC, in: 28th AIAA Applied Aerodynamics Conference, American Institute of Aeronautics and Astronautics Inc., Chicago, Illinios, 2010. doi:10.2514/6.2010-4393.

[25] D. D. Vicroy, T. D. Loeser, A. Schütte, SACCON Dynamic Wind Tunnel Tests at DNW-NWB and $14' \times 22'$ NASA LaRC, in: 28th AIAA Applied Aerodynamics Conference, American Institute of Aeronautics and Astronautics Inc., Chicago, Illinois, 2010. doi:10.2514/6.2010-4394.

[26] D. Rohlf, S. Schmidt, J. Irving, SACCON Stability and Control Analysis Applying System Identification Techniques, in: 28th AIAA Applied Aerodynamics Conference, American Institute of Aeronautics and Astronautics Inc., Chicago, Illinois, 2010. doi:10.2514/6.2010-4399.

[27] D. D. Vicroy, T. D. Loeser, A. Schütte, Static and Forced-Oscillation Tests of a Generic Unmanned Combat Air Vehicle, Journal of Aircraft 49 (6) (2012) 1558–1583. doi:10.2514/1.C031501.

[28] D. D. Vicroy, K. C. Huber, D. Rohlf, T. Löser, Low-speed Dynamic Wind Tunnel Test Analysis of a Generic 53° Swept UCAV Configuration with Controls, in: 32nd AIAA Applied Aerodynamics Conference, American Institute of Aeronautics and Astronautics Inc., Atlanta, Georgia, 2014. doi:10.2514/6.2014-2003.

[29] D. D. Vicroy, K. C. Huber, A. Schütte, M. Rein, J. P. Irving, G. Rigby, T. Löser, A.-R. Hübner, T. J. Birch, Experimental Investigations of a Generic Swept Unmanned Combat Air Vehicle with Controls, Journal of Aircraft 55 (2) (2016) 475–501. doi:10.2514/1.C033782.

[30] S. D. Carnduff, S. D. Erbsloeh, A. K. Cooke, M. V. Cook, Development of a low cost dynamic wind tunnel facility utilizing MEMS inertial sensors, in: 46th AIAA Aerospace Sciences Meeting and Exhibit, Reno, Nevada, 2008. doi:10.2514/6.2008-196.

[31] S. D. Carnduff, S. D. Erbsloeh, A. K. Cooke, M. V. Cook, Characterizing Stability and Control of Subscale Aircraft from Wind-Tunnel Dynamic Motion, Journal of Aircraft 46 (1) (2009) 137–147. doi:10.2514/1.36730.

[32] N. K. Peyada, A. K. Ghosh, T. H. Go, Mathematical modelling, simulation, and estimation of aircraft parameters using five degree-of-freedom dynamic test rig:, Proceedings of the Institution of Mechanical Engineers, Part G: Journal of Aerospace Engineering 226 (1) (2012) 55–63. doi:10.1177/0954410011407265.

[33] J. Pattinson, M. H. Lowenberg, M. G. Goman, Multi-Degree-of-Freedom Wind-Tunnel Maneuver Rig for Dynamic Simulation and Aero-

dynamic Model Identification, Journal of Aircraft 50 (2) (2013) 551–566. doi:10.2514/1.C031924.

[34] J. Pattinson, M. H. Lowenberg, M. G. Goman, Investigation of Poststall Pitch Oscillations of an Aircraft Wind-Tunnel Model, Journal of Aircraft 50 (6) (2013) 1843–1855. doi:10.2514/1.C032184.

[35] S. A. Araujo-Estrada, Control of a Wind Tunnel Manoeuvre-Rig to Physically Simulate Free-Flight Motion of an Aircraft Model, Phd thesis, University of Bristol (2016).

[36] S. A. Araujo-Estrada, Z. Gong, M. H. Lowenberg, S. Neild, M. Goman, Wind Tunnel Manoeuvre Rig: A Multi-DOF Test Platform for Model Aircraft, in: 54th AIAA Aerospace Sciences Meeting, 2016. doi:10.2514/6.2016-2119.

[37] S. A. Araujo-Estrada, M. H. Lowenberg, S. Neild, M. Goman, Evaluation of Aircraft Model Upset Behaviour Using Wind Tunnel Manoeuvre Rig, in: AIAA Atmospheric Flight Mechanics Conference, 2015, 2015. doi:10.2514/6.2015-0750.

[38] P. D. B. Navaratna, M. H. Lowenberg, S. A. Neild, Minimally Constrained Flight Simulation in Wind Tunnel, Journal of Aircraft 56 (4) (2019) 1–14. doi:10.2514/1.C035199.

[39] M. Tatar, M. Masdari, Investigation of pitch damping derivatives for the Standard Dynamic Model at high angles of attack using neural network, Aerospace Science and Technology 92 (2019) 685–695. doi:10.1016/j.ast.2019.06.046.

[40] T. Bykerk, D. Verstraete, J. Steelant, Low speed longitudinal dynamic stability analysis of a hypersonic waverider using unsteady Reynolds averaged Navier Stokes forced oscillation simulations, Aerospace Science and Technology 103 (2020) 105883. doi:10.1016/j.ast.2020.105883.

[41] Z. Gong, S. Araujo-Estrada, M. H. Lowenberg, S. A. Neild, M. G. Goman, Experimental Investigation of Aerodynamic Hysteresis Using a Five-Degree-of-Freedom Wind-Tunnel Maneuver Rig, Journal of Aircraft 56 (3) (2019) 1–11. doi:10.2514/1.C034995.

[42] H. Kyle, An investigation into the use of a pendulum support rig for aerodynamic modelling, Phd thesis, University of Bristol (2004).

[43] P. M. Davison, M. H. Lowenberg, M. di Bernardo, Experimental Analysis and Modeling of Limit Cycles in a Dynamic Wind-Tunnel Rig, Journal of Aircraft 40 (4) (2003) 776–785. doi:10.2514/2.3158.

[44] M. G. Goman, G. I. Zagainov, A. V. Khramtsovsky, Application of bifurcation methods to nonlinear flight dynamics problems, Progress in Aerospace Sciences 33 (9-10) (1997) 539–586. doi:10.1016/S0376-0421(97)00001-8.

[45] J.M.T Thompson, F.B.J. Macmillen (Eds.), Nonlinear Flight Dynamics of High-Performance Aircraft, Philosophical Transactions of the Royal Society A: Mathematical, Physical and Engineering Sciences 356 (1745) (1998). doi:10.1098/rsta.1998.0267.

[46] S. Sharma, E. B. Coetzee, M. H. Lowenberg, S. A. Neild, B. Krauskopf, Numerical continuation and bifurcation analysis in aircraft design: an

industrial perspective, Philosophical Transactions of the Royal Society A: Mathematical, Physical and Engineering Sciences 373 (2051) (2015). doi:10.1098/RSTA.2014.0406.

[47] R. V. Jategaonkar, Flight Vehicle System Identification: A Time Domain Methodology, American Institute of Aeronautics and Astronautics, 2006. doi:10.2514/4.866852.

[48] L. Renson, A. D. Shaw, D. A. Barton, S. A. Neild, Application of control-based continuation to a nonlinear structure with harmonically coupled modes, Mechanical Systems and Signal Processing 120 (2019) 449–464. doi:10.1016/J.YMSSP.2018.10.008.

[49] I. Tartaruga, D. Barton, D. Rezgui, S. Neild, Experimental bifurcation analysis of a wing profile, in: International Forum on Aeroelasticity and Structural Dynamics, Savannah, Georgia, 2019, pp. 1 –9.

[50] G.-g. Seo, Y. Kim, S. Saderla, Kalman-filter based online system identification of fixed-wing aircraft in upset condition, Aerospace Science and Technology 89 (2019) 307–317. doi:10.1016/j.ast.2019.04.012.

[51] F. Afonso, J. Vale, É. Oliveira, F. Lau, A. Suleman, A Review on Non-linear Aeroelasticity of High Aspect-ratio Wings, Progress in Aerospace Sciences 89 (2017) 40–57. doi:10.1016/j.paerosci.2016.12.004.

[52] W. He, T. Wang, X. He, L. J. Yang, O. Kaynak, Dynamical Modeling and Boundary Vibration Control of a Rigid-Flexible Wing System, IEEE/ASME Transactions on Mechatronics 25 (6) (2020) 2711–2721. doi:10.1109/TMECH.2020.2987963.

[53] W. He, X. Mu, L. Zhang, Y. Zou, Modeling and trajectory tracking control for flapping-wing micro aerial vehicles, IEEE/CAA Journal of Automatica Sinica 8 (1) (2021) 148–156. doi:10.1109/JAS.2020.1003417.

[54] T. Fleischer, S. Meyer-Soylu, J. Schippl, M. Decker, Personal aerial transportation systems (PATS) – A potential solution for the urban mobility challenges?, Futures 109 (2019) 50–62. doi:10.1016/j.futures.2019.03.006.

[55] E. Bohn, E. M. Coates, S. Moe, T. A. Johansen, Deep reinforcement learning attitude control of fixed-wing UAVs using proximal policy optimization, in: 2019 International Conference on Unmanned Aircraft Systems, ICUAS 2019, Institute of Electrical and Electronics Engineers Inc., 2019, pp. 523–533. doi:10.1109/ICUAS.2019.8798254.

[56] D. Wada, S. A. Araujo-Estrada, S. Windsor, Unmanned Aerial Vehicle Pitch Control Using Deep Reinforcement Learning with Discrete Actions in Wind Tunnel Test, Aerospace 8 (1) (2021) 18. doi:10.3390/aerospace8010018.